RSC Advances

PAPER

View Article Online
View Journal | View Issue

Cite this: *RSC Adv.*, 2025, **15**, 40174

Fabrication of a 3D/0D S-scheme heterojunction based on ZnO nanoflowers and $ZnIn_2S_4$ nanoparticles with enhanced CO_2 photoreduction performance

Jiaze Wang,†[ab] Tongbin Zhang,†[ab] Xiaoyan Liu,*[ab] Lili Yang,[ab] Jian Cao,[ab] Qiong Wu,[ab] Fengyou Wang,[ab] Yanli Chen,[ab] Xin Li*[ab] and Maobin Wei*[ab]

To address the challenges of easy agglomeration, inadequate adsorption capacity, and low electron separation efficiency of pure $ZnIn_2S_4$ during the CO_2 photoreduction process, a novel 3D/0D ZnO/$ZnIn_2S_4$ S-scheme heterojunction was fabricated by growing $ZnIn_2S_4$ nanoparticles (NPs) *in situ* on the surfaces of ZnO nanoflowers (NFs). By regulating the loading amount of $ZnIn_2S_4$ NPs, ZnO/$ZnIn_2S_4$ composites with high catalytic activity were obtained. The optimal performance was observed for the sample ZZ8 ($ZnIn_2S_4$: ZnO = 8 : 100 molar ratio), achieving the maximum CO_2 photoreduction rates. Under 4 h UV-vis light irradiation, ZZ8 produced CO and CH_4 of 149.38 μmol g^{-1} and 94.39 μmol g^{-1}, respectively, corresponding to 3.44 times and 5.51 times the rates of pure $ZnIn_2S_4$. The optimal $ZnIn_2S_4$ loading significantly expanded ZZ8's effective adsorption area and pore structure, enhancing CO_2 adsorption, activation and reactant diffusion. Concurrently, Zn–In bimetallic sites markedly boosted CO_2 adsorption and activation capacity, inducing a synergistic catalytic effect. After 10 reaction cycles, the CO production rate remained above 85%, indicating excellent photostability of ZZ8. Comprehensive analysis confirmed an S-scheme electron transfer pathway in the ZnO/$ZnIn_2S_4$ composite during CO_2 photoreduction, enabling efficient spatial separation of photogenerated charges. This study effectively optimized the photocatalytic performance of the material through morphology control and the construction of an S-scheme heterojunction. It provides a theoretical basis and a technical pathway for the rational design of other 3D/0D S-scheme heterojunction photocatalytic materials (*e.g.*, ZnO/g-C_3N_4, ZnO/MoS_2).

Received 28th August 2025
Accepted 16th October 2025

DOI: 10.1039/d5ra06450c

rsc.li/rsc-advances

1. Introduction

With the continuous advancement of global industrialization and commercialization, along with sustained population growth, fossil fuels are being excessively consumed. This has not only triggered an energy crisis but also led to serious emissions of the greenhouse gas carbon dioxide (CO_2). The continuous rise in atmospheric CO_2 concentrations has resulted in a series of serious ecological consequences, such as an increase in the global average temperature, ocean acidification, and intensified desertification.[1–4] At present, solar-powered photocatalytic CO_2 conversion into hydrocarbon fuels (*e.g.*, CO, CH_4, and CH_3OH) offers a highly promising route to carbon neutrality.[5–7] This technology involves key steps such as light absorption, carrier separation, surface adsorption of CO_2, catalytic conversion and complex multi-electron transfer processes. In addition, to achieve efficient CO_2 reduction, the photocatalyst must have appropriate conduction band (CB) and valence band (VB) potentials to generate charge carriers powerful enough to break CO_2's stable C=O bonds.

Zinc indium sulfide ($ZnIn_2S_4$), as a bimetallic sulfide, possesses advantages such as a tunable band gap (2.06–2.85 eV), strong visible-light responsiveness, controllable morphology, high chemical stability, and low toxicity, making it an ideal semiconductor material for photocatalytic CO_2 reduction.[8–10] However, the single-component $ZnIn_2S_4$ semiconductor suffers from issues such as easy agglomeration, high recombination rate of surface photogenerated carriers, inadequate CO_2 adsorption and activation capabilities, and limited visible-light response range, resulting in low photocatalytic activity and hindering its practical applications. To address these issues, researchers have developed multiple optimization approaches, including morphology modulation, defect engineering, ion doping, surface plasmonic modification, and heterostructure

[a]*Key Laboratory of Functional Material Physics and Chemistry of the Ministry of Education, Jilin Normal University, Changchun 130103, PR China. E-mail: liuxiaoyan1437@163.com; xlwl@jlnu.edu.cn; jlsdzccw@126.com*

[b]*National Demonstration Center for Experimental Physics Education, Jilin Normal University, Siping 136000, PR China*

† The authors have the equal contribution to the manuscript.

construction.[11–14] Among these, constructing heterojunctions is a highly promising solution. Selecting suitable semiconductor materials can not only enhance the dispersion of the host material, expose more active sites, and broaden the spectral response range, but also facilitate the efficient spatial separation of photogenerated carriers.

In recent years, the construction of S-scheme heterojunctions, which combine a reduction photocatalyst (RP) and an oxidation photocatalyst (OP), has become a well-established effective strategy. Under illumination, this architecture facilitates interfacial recombination between CB's electrons of the lower Fermi level (E_f) semiconductor and VB's holes of the higher E_f semiconductor through the built internal electric field (IEF) and induced band bending. This unique charge transfer mechanism effectively inhibits the carrier recombination within the individual component while retaining high-energy electrons and holes.[5,15] Consequently, it can simultaneously fulfill the requirements for both oxidation and reduction reactions. We have successfully loaded 2D RP $ZnIn_2S_4$ nanosheets onto 2D OP WO_3 nanosheets for efficient CO_2 photoreduction. This unique 2D/2D S-scheme heterostructure can form intimate interfacial contact, effectively promoting interfacial charge transfer.[16] Therefore, the selection of RP and OP semiconductor materials, which possess specific nanostructures, matched band structures, and appropriate E_f positions, is critical to constructing high-efficiency S-scheme nanocatalysts.

Zinc oxide (ZnO), as a typical OP semiconductor photocatalyst, is extensively applied in photocatalysis, benefiting from its non-toxicity, morphological diversity, low cost, environmental compatibility, and strong oxidation ability.[17–19] However, the inherent wide bandgap property of ZnO (~3.37 eV) severely limits its light absorption range (utilizing only 3–5% of the solar spectrum), leading to poor solar energy utilization.[20–22] $ZnIn_2S_4$ and ZnO share the same metal element (Zn) and exhibit well-matched band structures. When the two are combined, it is expected to form an intimate interfacial contact and an S-scheme charge transfer pathway, thereby broadening their spectral response range and enhancing their photocatalytic activity. On the other hand, 3D hierarchical micro-nano oxide structures, constructed from building blocks such as nanoparticles, nanorods, or nanosheets, have garnered significant scientific interest owing to their unique structural configurations and tunable material properties (*e.g.*, low agglomeration, high specific surface area, well-ordered porous structure).[23,24] These characteristics endow them with promising application prospects in the field of photocatalysis.

Herein, hierarchical 3D flower-like ZnO nanostructures assembled from tightly interwoven nanosheets were prepared *via* a solvothermal method. Subsequently, 0D $ZnIn_2S_4$ nanoparticles (NPs) were *in situ* grown onto the ZnO nanoflowers (NFs), resulting in a 3D/0D ZnO/$ZnIn_2S_4$ S-scheme heterojunction. This unique structure not only effectively suppresses the agglomeration of $ZnIn_2S_4$ NPs but also maximally exposes their photoreduction sites, thereby enhancing their CO_2 adsorption capacity and achieving efficient spatial separation of photogenerated charge carriers. Under UV-vis irradiation, the ZZ8 sample exhibited significantly enhanced CO and CH_4 production rates compared to pure ZnO and $ZnIn_2S_4$. The S-scheme charge transfer mechanism was systematically elucidated through comprehensive photoelectrochemical and spectroscopic characterization. Additionally, *in situ* FTIR spectroscopy was employed to probe the reaction pathway of photocatalytic CO_2 reduction.

2. Experimental section

2.1 Chemicals

Zinc acetate dihydrate ($Zn(CH_3COO)_2 \cdot 2H_2O$, AR, ≥99.0%), sodium hydroxide (NaOH, AR, ≥96.0%), anhydrous sodium sulfate (Na_2SO_4, AR, ≥99.0%), zinc chloride ($ZnCl_2$, AR, ≥98.0%), ethylene glycol ($C_2H_6O_2$, AR, ≥99.5%), and absolute ethyl alcohol (C_2H_5OH, ≥99.7%) were sourced from Sinopharm Chemical Reagent Co., Ltd. Indium(III) chloride tetrahydrate ($InCl_3 \cdot 4H_2O$, ≥99.9% metals basis) and thioacetamide (TAA, C_2H_5NS, ACS, ≥99.0%) were obtained from Shanghai Aladdin Biochemical Technology Co., Ltd, while glycine ($C_2H_5NO_2$, BR, 99%) was provided by Beijing InnoChem Science & Technology Co., Ltd.

The detailed testing procedures, instrument models and manufacturers are provided in the SI.

2.2 Preparation of ZnO nanoflowers

ZnO nanoflowers (NFs) were synthesized *via* the solvothermal method.[23] First, 0.75 g of $Zn(CH_3COO)_2 \cdot 2H_2O$ was dissolved in a 30 mL deionized water and 20 mL C_2H_5OH mixed solvent under vigorous stirring at 25 °C. Subsequently, 1.2 g of $C_2H_5NO_2$ and 1.2 g of Na_2SO_4 were added stepwise, with each addition followed by 10 min of continuous stirring. Then, the mixture was basified *via* dropwise addition of 20 mL NaOH (1.5 M) solution, stirred for 10 min to homogenize, and transferred to a 100 mL Teflon-lined autoclave. The sealed reactor was kept at 140 °C for 18 h in an electric oven. Following natural cooling to ambient temperature, the product was isolated by centrifugation, rigorously washed with C_2H_5OH and deionized water, and vacuum-dried at 60 °C for 12 h to obtain pure ZnO NFs.

2.3 Preparation of ZnO/$ZnIn_2S_4$ nanocomposites

ZnO/$ZnIn_2S_4$ nanocomposites were constructed by *in situ* growth method. First, ZnO NFs (2.6 mmol) were uniformly dispersed in 25 mL of $C_2H_6O_2$ by stirring 10 min with ultrasonic assistance. Subsequently, stoichiometric amounts of $ZnCl_2$ (0.156 mmol), $InCl_3 \cdot 4H_2O$ (0.312 mmol), and TAA (0.624 mmol) were added sequentially to the suspension under ultrasonic stirring. Then, the mixture was sealed in a 100 mL Teflon-lined autoclave and subjected to hydrothermal treatment at 120 °C for 2 h. Upon natural cooling to room temperature, the yellow precipitates were collected, followed by six cycles of alternating washing with C_2H_5OH and deionized water to eliminate residual impurities. The purified sample was vacuum-dried at 60 °C overnight to yield the 6% ZnO/$ZnIn_2S_4$ nanocomposites (ZZ6; molar ratio $ZnIn_2S_4$: ZnO = 6 : 100). Using identical synthesis parameters while varying precursor ratios, we fabricated a series of composites with $ZnIn_2S_4$ NPs loadings of 8%,

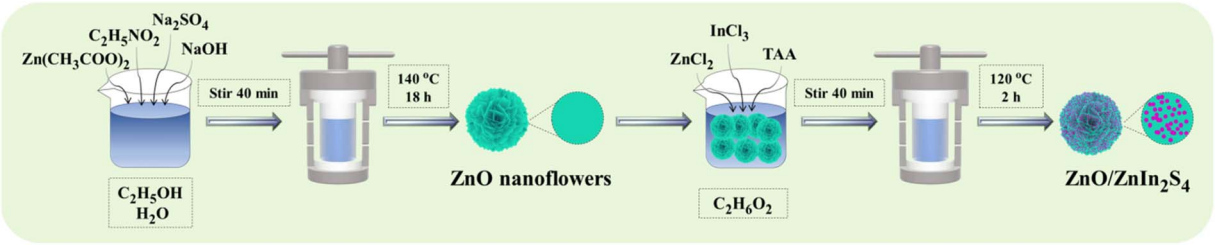

Scheme 1 Schematic illustration of the *in situ* growth process for $ZnO/ZnIn_2S_4$ nanocomposites.

10%, and 12% (ZZ8, ZZ10, ZZ12 corresponding to molar ratios 8 : 100, 10 : 100, 12 : 100). The complete fabrication workflow is illustrated in Scheme 1.

For comparative analysis, pure $ZnIn_2S_4$ was synthesized using identical reaction conditions in the absence of ZnO.[20]

3. Results and discussion

3.1 Structural and morphological characterization

XRD was initially employed to analyze the crystalline phase structures and compositional characteristics. As depicted in Fig. 1(a), pure ZnO presents diffraction peaks consistent with the hexagonal wurtzite ZnO (JCPDS: 36-1451). The peaks observed at approximately $2\theta = 31.8°$, 34.4°, 36.3°, 47.5°, 56.6°, 62.9°, and 68.0° are indexed to the (100), (002), (101), (102), (110), (103), and (112) planes, respectively.[15,23,25] Similarly, pure $ZnIn_2S_4$ displays distinct hexagonal phase peaks (JCPDS: 72-0773) at around $2\theta = 21.6°$, 27.8°, 30.4°, and 47.5°, assigned to the (006), (102), (104), and (110) planes, respectively.[26,27] The XRD pattern of pure $ZnIn_2S_4$ shows broadened peaks, indicating poor crystallinity. Notably, ZZ8 composite clearly reveals coexisting diffraction peaks from both ZnO and $ZnIn_2S_4$ phases (Fig. S1(a)), indicating the successful loading of $ZnIn_2S_4$ onto ZnO. Compared with the XRD patterns of the composites (Fig. 1(b)), it can be found that the diffraction peaks associated with ZnO gradually weaken from ZZ6 to ZZ12. Concurrently, the intensity ratio of $ZnIn_2S_4$ to ZnO diffraction peaks shows an increasing trend (Fig. S1(b)), indicating a growing amount of $ZnIn_2S_4$ onto the ZnO surface. Moreover, no diffraction peaks attributable to impurity phases were detected, confirming the high purity of all synthesized composites.

XPS analyses were performed on ZnO, $ZnIn_2S_4$ and ZnO/$ZnIn_2S_4$ composites to examine their surface elemental chemical states and atomic compositions. All spectra were calibrated against the C 1s reference peak (284.8 eV).[28] Full survey spectra verify the presence of Zn, O, In, and S in sample ZZ8 without detectable impurities (Fig. S2), confirming the successful deposition of $ZnIn_2S_4$ onto ZnO. The Zn 2p high-resolution spectrum of pure ZnO (Fig. 1(c)) shows peaks at 1044.58 eV (Zn $2p_{1/2}$) and 1021.52 eV (Zn $2p_{3/2}$), characteristic of Zn^{2+}.[12] In contrast, pure $ZnIn_2S_4$ exhibits Zn $2p_{1/2}$ and Zn $2p_{3/2}$ peaks at 1044.91 eV and 1021.85 eV, respectively. The Zn 2p peaks of ZZ8 composite exhibit noticeable asymmetry and can be deconvoluted into two distinct peaks, indicating different electronic environments around Zn atoms in the composite.[29] The dominant signals at 1044.49 eV and 1021.49 eV are assigned to Zn^{2+} in ZnO ($2p_{1/2}$ and $2p_{3/2}$, respectively). Concurrently, lower-intensity peaks at 1045.72 eV and 1022.56 eV arise from Zn^{2+} in $ZnIn_2S_4$.[21]

The In 3d spectrum of pure $ZnIn_2S_4$ (Fig. 1(d)) reveals characteristic In^{3+} states at 452.36 eV ($3d_{3/2}$) and 444.79 eV ($3d_{5/2}$).[12] Similarly, S 2p peaks at 162.59 eV ($2p_{1/2}$) and 161.40 eV ($2p_{3/2}$) in Fig. 1(e) confirm the S^{2-} chemical state.[13] Together with the Zn 2p data, these spectra confirm the successful synthesis of $ZnIn_2S_4$. The deconvoluted O 1s spectrum of ZnO (Fig. 1(f)) exhibits peaks at 530.41 eV (lattice oxygen, O–Zn), 532.36 eV (adsorbed oxygen), and 533.92 eV (adsorbed water).[26,30] Compared to pure ZnO NFs, the O–Zn peak is suppressed after $ZnIn_2S_4$ shell growth. In the photoreduction of CO_2 reaction, adsorbed oxygen and water are essential, the increased proportion of them in ZZ8 indicates enhanced redox capacity of the composite material.[26] The composite formed between ZnO and $ZnIn_2S_4$ exhibits distinct peak shifts compared to its individual components. Compared to pure $ZnIn_2S_4$, the characteristic Zn, In, and S peaks in ZZ8 shift marginally toward higher binding energies, indicating reduced electron density in $ZnIn_2S_4$. In contrast to pure ZnO, the Zn and O elements in the ZZ8 sample shift toward lower binding energies, indicating that ZnO gains electrons. These observations collectively demonstrate that electrons spontaneously transfer from $ZnIn_2S_4$ to ZnO in the composite material under dark conditions.[31,32] This reveals strong interfacial coupling and electronic interaction between ZnO and $ZnIn_2S_4$, providing crucial experimental evidence for elucidating the charge transfer mechanism in heterostructures.[28,33]

Surface functional groups and chemical composition were characterized by FTIR (Fig. S3). The spectrum of pure $ZnIn_2S_4$ shows broad absorptions at 3430, 1629, and 1397 cm^{-1}, assigned to the vibrational modes of surface-absorbed H_2O molecules or hydroxyl groups.[34,35] C–H bending (3003–2800 cm^{-1}) and C–N stretching (1171–1016 cm^{-1}) modes are observed. The pure ZnO exhibits two Zn–O vibrational bands between 600–350 cm^{-1}.[36] The sample ZZ8 retains these characteristic modes of the individual components, confirming the formation of ZnO/$ZnIn_2S_4$ heterostructure at the molecular vibrational level.

SEM and TEM characterization were employed to reveal the sample's microstructure and morphology. Fig. 2(a) shows that the hierarchical 3D flower-like nanostructures of pure ZnO NFs are composed of tightly overlapped and interwoven nanosheets.

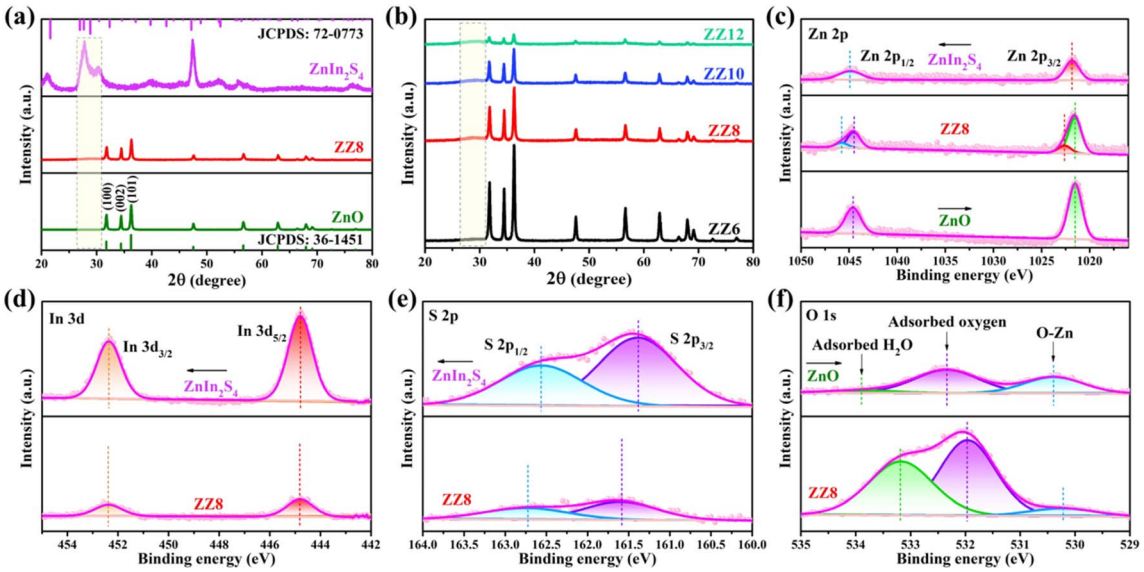

Fig. 1 XRD patterns (a and b) and XPS spectra (c–f) of the samples.

A locally magnified view (Fig. 2(b)) shows the ZnO nanosheets (NSs) have smooth surfaces and thicknesses of 50–60 nm. Fig. S4(a) displays a nanoflower morphology of pure $ZnIn_2S_4$, self-assembled from ultrathin nanosheets. In the SEM image of ZZ8 composite (Fig. 2(c)), $ZnIn_2S_4$ exists as tiny nanoparticles attached to the surface of ZnO NSs, while the overall flower-like microstructure of the ZnO NFs remains largely intact. During the *in situ* synthesis of the nanocomposite, the interaction of Zn^{2+} and In^{3+} ions with atoms on the ZnO NFs facilitates the direct growth of $ZnIn_2S_4$ NPs on the ZnO NSs.[26,37] Consequently, the resulting morphology of $ZnIn_2S_4$ in ZZ8 composite differs significantly from that of pure $ZnIn_2S_4$. The successful loading of these particulate $ZnIn_2S_4$ nanostructures provides abundant catalytically active sites. The intimate contact between $ZnIn_2S_4$ NPs and ZnO NSs in ZZ8 is confirmed by the high-magnification SEM (Fig. 2(d)), which shows a roughened nanosheet surface. This interaction creates a coarse, shell-like coating that should facilitate rapid migration of photogenerated charge carriers for enhanced photocatalysis.[20]

As shown in Fig. S5, the morphology of the composites (ZZ6, ZZ8, ZZ10 and ZZ12) changes significantly with the increasing concentration of $ZnIn_2S_4$, accompanied by a rise in the number of particles on the nanosheet surfaces. In the ZZ12 sample, the ZnO nanoflower structure is almost entirely covered by $ZnIn_2S_4$ NPs, and the original morphology becomes indistinguishable. The excessive $ZnIn_2S_4$ coverage can block the active sites and hinder the access of light and reactants to the ZnO/$ZnIn_2S_4$ interface. This morphological evolution provides critical evidence for establishing the structure–property relationship of the materials. The EDS spectrum of ZZ8 (Fig. S6(a)) further confirms the presence of Zn, O, In, and S elements in the composite. Additionally, the homogeneous distribution of these constituent elements throughout the composite, evident from the elemental mapping in Fig. 2(e), indicates that the two

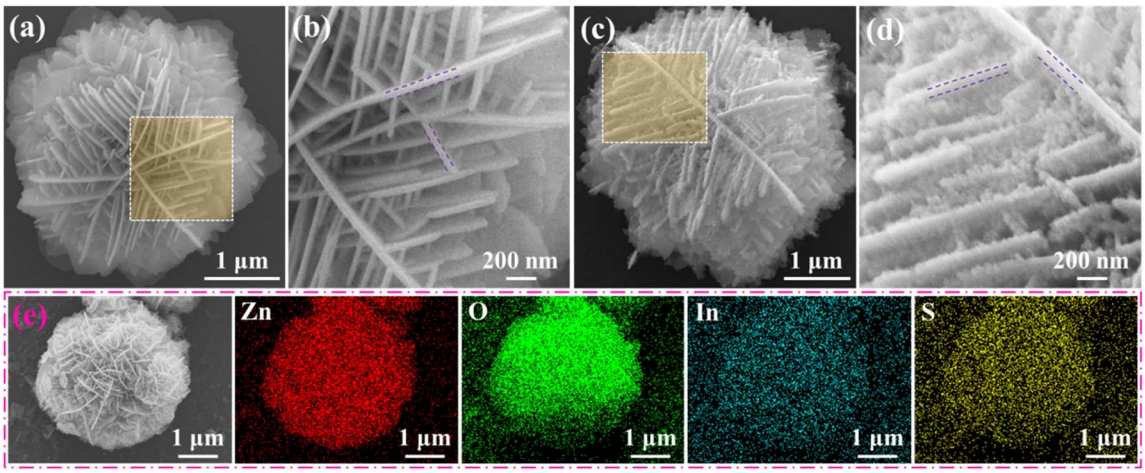

Fig. 2 SEM images of pure ZnO (a and b) and ZZ8 (c and d); elemental mapping images of ZZ8 (e).

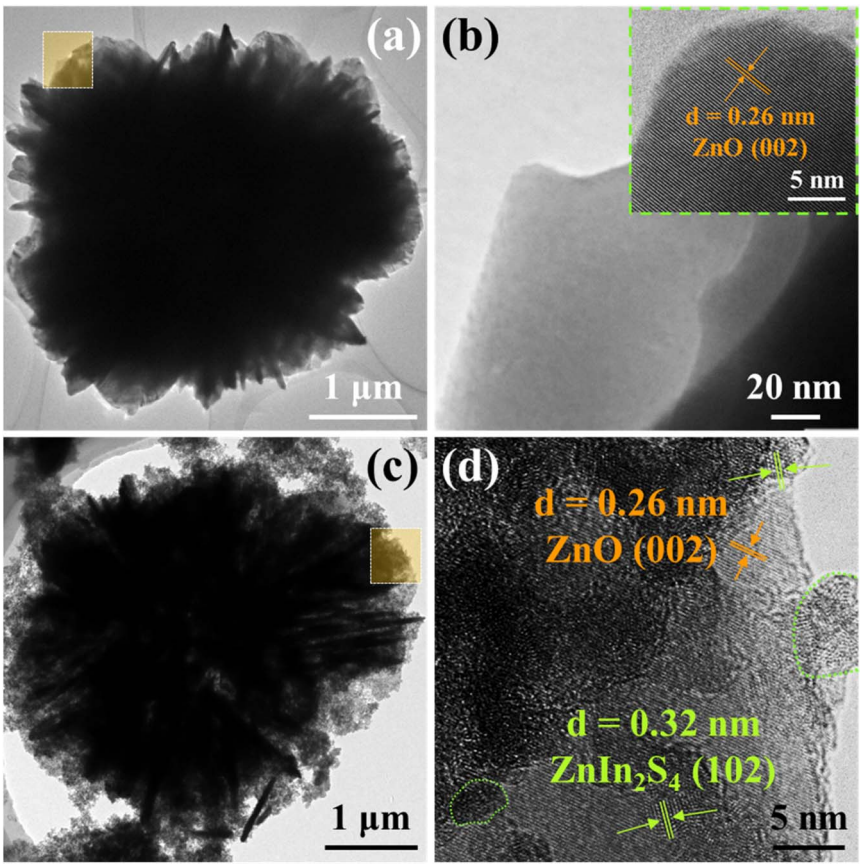

Fig. 3 TEM images of pure ZnO (a and b) and ZZ8 (c and d).

semiconductor materials are intimately integrated.[14,27,38] This optimized interfacial structure is anticipated to enhance charge separation, thereby boosting photocatalytic performance.

The morphological features observed by SEM are further verified in the corresponding TEM images (Fig. 3(a, c) and S4(b)) for pure ZnO, pure $ZnIn_2S_4$, and ZZ8. Notably, Fig. 3(b) reveals the exceptionally smooth nanosheet surfaces of pure ZnO NFs. The well-ordered lattice fringes with a measured spacing of 0.26 nm are visible in the HRTEM image (the inset of Fig. 3(b)), consistent with the ZnO (002) plane.[39] As seen in Fig. S4(c), pure $ZnIn_2S_4$ exhibits poor crystallinity, with lattice fringes measuring 0.32 nm corresponding to its (102) plane.[26] Significant changes in brightness contrast can be observed in the HRTEM image of the ZZ8 composite (Fig. 3(d)), which confirms that $ZnIn_2S_4$ NPs have anchored onto ZnO NSs, forming a rough surface. The average particle size of $ZnIn_2S_4$ NPs is approximately 5 nm (Fig. S6(b)). The coexisting 0.26 nm (ZnO (002)) and 0.32 nm ($ZnIn_2S_4$ (102)) lattice fringes in Fig. 3(d) unambiguously verifies the formation of the ZnO/$ZnIn_2S_4$ heterojunction interface. These findings are consistent with the XRD and XPS results, confirming the effective formation of the ZnO/$ZnIn_2S_4$ heterojunction.

3.2 CO_2 photoreduction performance analysis

Systematic evaluation of photocatalytic CO_2 reduction performance was conducted under UV-vis irradiation without sacrificial agents. As shown in Fig. 4(a and b), the gaseous products are predominantly composed of CO and CH_4. After 4 h of irradiation, CO and CH_4 yields reach 45.01 and 3.45 μmol g^{-1} for pure ZnO, respectively, while pure $ZnIn_2S_4$ produces 43.46 μmol per g CO and 17.12 μmol per g CH_4. In contrast, the ZZ8 composite demonstrates significantly enhanced catalytic activity, with CO and CH_4 yields reaching 149.38 and 94.39 μmol g^{-1}, respectively. Quantitative analysis reveals that the CO yield of the ZZ8 composite is 3.32 times that of pure ZnO and 3.44 times that of pure $ZnIn_2S_4$. More strikingly, the CH_4 yield exhibits a substantially greater enhancement, reaching 27.36 times the value of ZnO and 5.51 times that of $ZnIn_2S_4$. According to the comparison results in Table S1, it can be seen that compared with the ZnO-based and $ZnIn_2S_4$-based composite materials reported in the literature, the ZnO/$ZnIn_2S_4$ sample synthesized in this study also has significant advantages in the photoreduction of CO_2 to CH_4. As the loading amount of $ZnIn_2S_4$ increases, CO and CH_4 yields first rise then fall in the composites (Fig. 4(b)), exhibiting characteristic volcano-type behavior. The activity maximum is observed for ZZ8, demonstrating the decisive role of compositional control in activity enhancement. Combining SEM and performance results, it is evident that excessive loading of $ZnIn_2S_4$ hinders light penetration at the ZnO/$ZnIn_2S_4$ interface and impedes CO_2 access to active sites.[40]

Furthermore, the utilization rate (R) of photogenerated electrons can directly reflect the sample's photoreduction

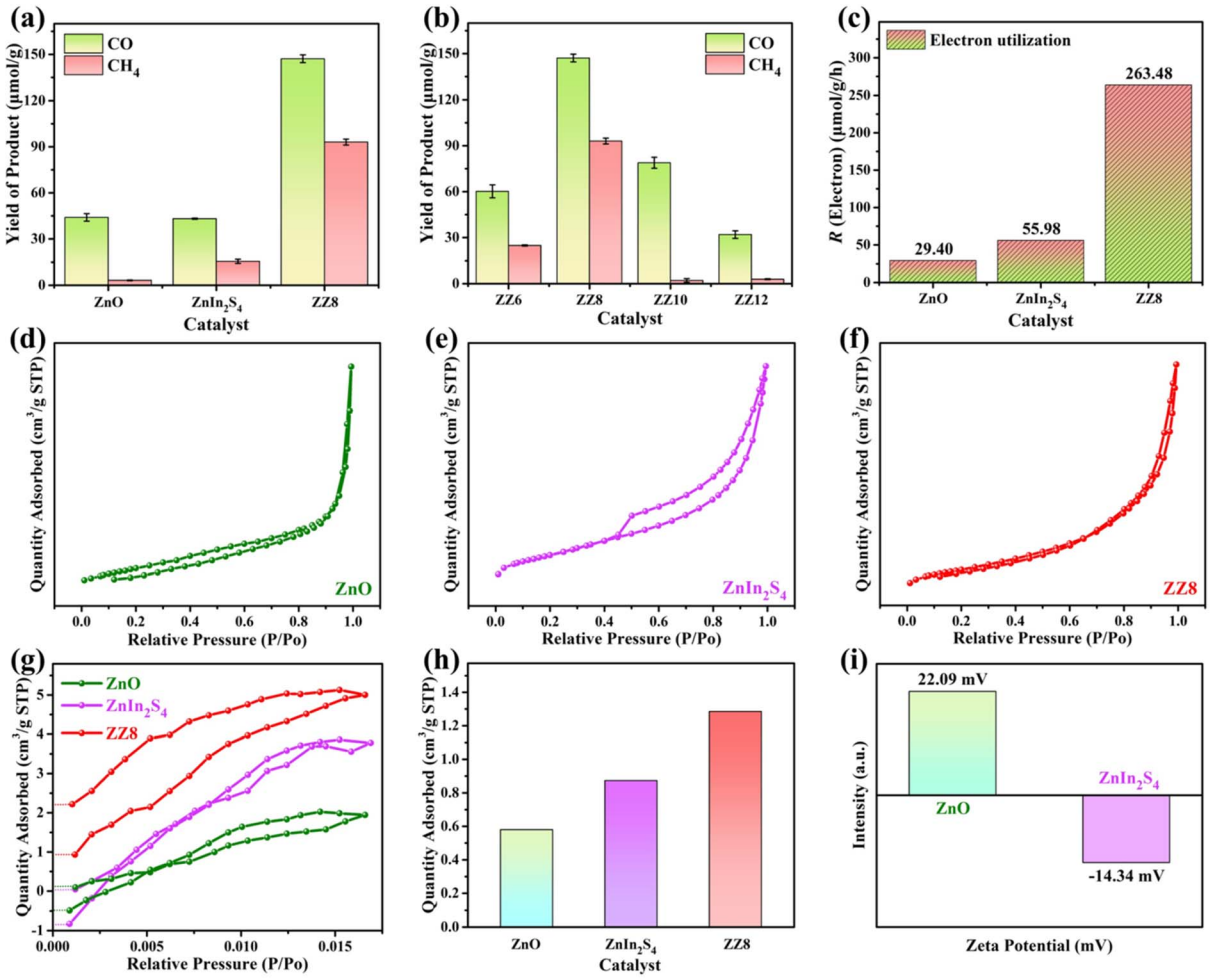

Fig. 4 (a–c) CO_2 photoreduction activity, (d–f) N_2 adsorption–desorption isotherms, (g–h) CO_2 adsorption–desorption isotherms with corresponding net adsorption histogram, and (i) zeta potentials of the samples.

capability for CO_2.[41] ZZ8 shows a calculated electron utilization rate of 263.48 μmol g^{-1} h^{-1} (Fig. 4(c)), significantly higher than those of pure ZnO (29.40 μmol g^{-1} h^{-1}) and $ZnIn_2S_4$ (55.98 μmol g^{-1} h^{-1}). This substantial enhancement further evidences ZZ8's superior CO_2 photoreduction performance. Based on the yields, the product and electron selectivity for CO and CH_4 of the samples were calculated (Fig. S7(a and b)).[42] The ZZ8 composite exhibits a notable enhancement in CH_4 selectivity, confirming that the ZnO/$ZnIn_2S_4$ heterojunction effectively facilitates charge transfer. This process increases the surface electron density, which promotes the protonation of reaction intermediates and ultimately leads to higher CH_4 selectivity. As shown in Fig. S7(c) and Table S2, the apparent quantum efficiency (AQE) of the ZZ8 composite is about 3.03% at 360 nm, 0.28% at 420 nm, 0.07% at 500 nm, 0.06% at 550 nm, respectively. This wavelength-dependent trend in AQE correlates with the light absorption edge of ZZ8, confirming that the CO_2 reduction is a light-driven process.[43] To identify the carbon source in reduction products, control experiments were operated under three conditions: (i) without light, (ii) without catalyst, and (iii) replace CO_2 with Ar. The null product detection in control experiments (Fig. S7(d)) establishes catalyst-driven CO_2 photoreduction as the exclusive origin of carbon-based products. As stability evaluation is essential for photocatalyst assessment, ZZ8 underwent ten cyclic CO_2 reduction tests (Fig. S8(a)). Between runs, the reaction system was thoroughly cleaned and the recovered catalyst was degassed. After ten consecutive cycles, the CO production rate decreases only marginally from 149.38 to 129.57 μmol g^{-1}. The XRD, XPS and SEM analyses (Fig. S8(b–d)) reveal no significant changes in the crystalline structure, element composition or morphology of ZZ8 after 10 runs.[44,45] These results confirm the concurrent achievement of exceptional photostability and high catalytic activity in the ZZ8 composite.

To elucidate the role of the surface structural characteristics in photocatalytic performance, we conducted N_2 and CO_2 adsorption–desorption analyses. The N_2 adsorption–desorption isotherms were used to determine the specific surface areas and pore size distributions (Fig. 4(d–f) and S9).[46] Pure ZnO, $ZnIn_2S_4$, and ZZ8 all exhibit IV-type isotherms with H3-type hysteresis loops. ZnO displays typical mesoporous characteristics, while $ZnIn_2S_4$ and the ZZ8 composite show hierarchical porous structures combining mesopores and macropores.[27] According to Brunauer–Emmett–Teller (BET) measurements (Table S3),

a specific surface area of 87.48 m^2 g^{-1} is achieved for the optimized ZZ8 composite, representing 5.82-fold and 1.95-fold increases compared to pure ZnO (15.04 m^2 g^{-1}) and $ZnIn_2S_4$ (44.96 m^2 g^{-1}), respectively. The significantly enhanced specific surface area not only provides more active sites for photocatalytic reactions but also substantially improves the transport efficiency of photogenerated charge carriers during redox processes.[47] This further promotes CO_2 capture and activation, thereby greatly enhancing the photocatalytic performance of the material. Additionally, ZZ8 demonstrates a significantly improved pore volume (0.32 cm^3 g^{-1}) compared to its individual components. This hierarchical porous structure provides an ideal three-dimensional mass transfer pathway for reactant diffusion and accessibility to active sites.

From the CO_2 adsorption–desorption isotherms (Fig. 4(g)), the ZZ8 composite demonstrates a significantly enhanced CO_2 capture capability compared to pure ZnO and $ZnIn_2S_4$. When the pressure was restored to ambient conditions, the adsorbed CO_2 molecules were not completely desorbed, confirming that a large amount of CO_2 was strongly bound and retained on the catalyst surface. The net CO_2 adsorption capacity of ZZ8 was calculated to be approximately 1.29 cm^3 g^{-1} (Fig. 4(h)), representing about a 2.22-fold increase over pure ZnO. The superior CO_2 capture performance of ZZ8 primarily originates from two aspects: first, the loaded $ZnIn_2S_4$ NPs form "nanoscale protrusions" on the surface of ZnO NSs, transforming the originally smooth nanosheets into a three-dimensional interface with subnanometer-scale roughness. This markedly expands the accessible surface area and optimizes the pore structure, resulting in a greater number of exposed catalytic sites that facilitate CO_2 capture. Second, the introduction of bimetallic active sites (Zn–In) significantly enhances the material's adsorption and activation capabilities toward the target CO_2 molecules, creating a synergistic effect that promotes subsequent catalytic conversion.

To further investigate the surface charge characteristic of the catalyst, zeta potential measurement was conducted to analyze the electrostatic interaction between the components (Fig. 4(i)). The results show that the Zeta potentials of ZnO and $ZnIn_2S_4$ in aqueous solution are +22.09 mV and −14.34 mV, respectively. This significant opposite charge distribution provides the driving force for the formation of heterojunction. The deposition of negatively charged $ZnIn_2S_4$ onto ZnO NSs will significantly enhance the catalyst's adsorption capability toward the electro-deficient carbon atoms in CO_2, thereby improving its CO_2 capture capacity. These findings align with the results obtained from the CO_2 adsorption–desorption isotherms.

3.3 Photoelectrochemical characterization

In order to elucidate the separation, transport, and recombination kinetics of photogenerated electron–hole pairs, the synthesized catalysts were subjected to a comprehensive set of photoelectrochemical analyses, including TPR, EIS, PL, LSV, and TRPL. TPR tests were performed under multiple on-off

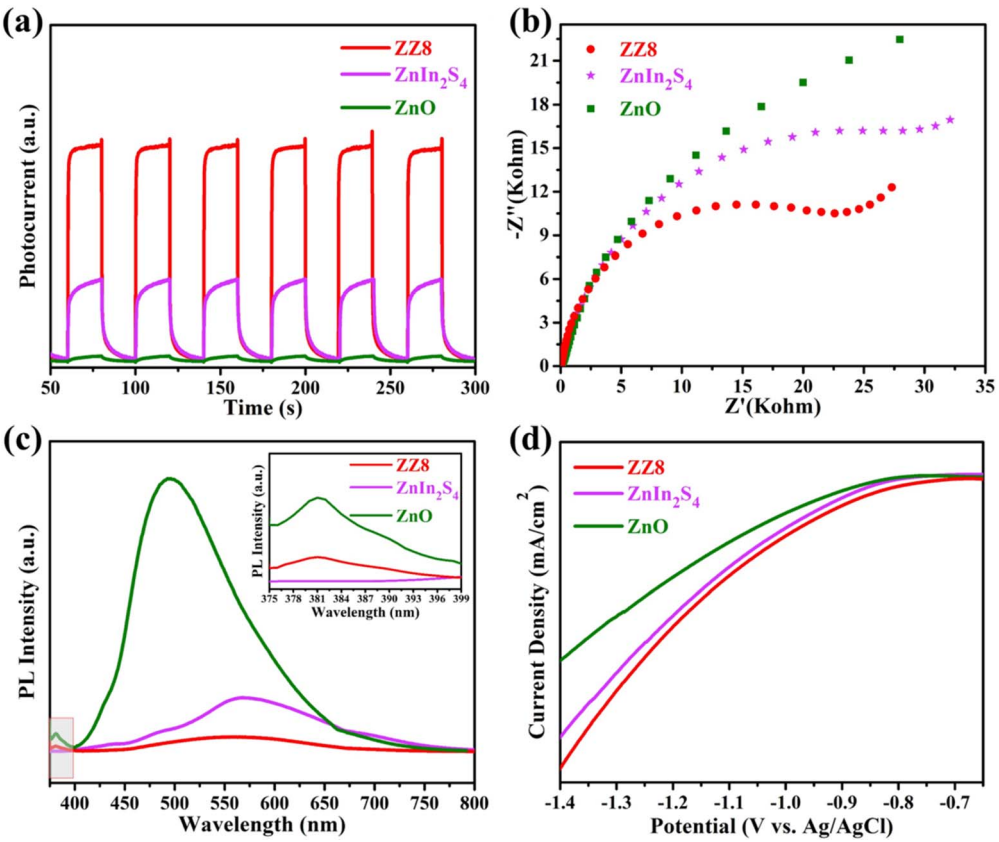

Fig. 5 (a) TPR curves, (b) EIS plots, (c) PL spectra, and (d) LSV curves of the samples.

illumination cycles. As illustrated in Fig. 5(a), all tested samples display stable and sensitive photocurrent responses during each switching cycle. It is widely acknowledged that stronger photocurrent peaks correspond to more efficient separation of photogenerated charge carriers in the photocatalysts.[12,48] Pure ZnO and $ZnIn_2S_4$ demonstrate relatively low photocurrent responses, while the ZZ8 composite shows a significantly improved photocurrent response. This strongly demonstrates that the constructed ZnO/$ZnIn_2S_4$ heterojunction effectively suppresses the recombination of photogenerated charge carriers while promoting the rapid transfer of photogenerated electrons, thereby achieving optimal interfacial charge transfer capability.[40] The photocurrent intensity of the sample shows a positive correlation with its photocatalytic performance. The ZZ8 composite, which exhibits the best CO_2 photoreduction performance, displays the strongest photocurrent response as expected. This conclusion was further confirmed by the EIS experimental results. The EIS plots (Fig. 5(b)) show that the ZZ8 composite has a significantly smaller arc radius in the intermediate-frequency region than any single component. This indicates a lower charge transfer resistance, which facilitates the migration of photogenerated charge carriers and thereby enhances photocatalytic performance.[49–51]

As shown in Fig. 5(c), the PL spectrum of pure ZnO exhibits a distinct intrinsic emission peak at ~382 nm and a broad defect-related band spanning from 400 to 750 nm. For pure $ZnIn_2S_4$, a clear band-edge emission peak is observed around 570 nm.[30,52] The intrinsic emission, a signature of radiative free exciton recombination, increases in peak intensity, suggesting an enhanced recombination rate of the photogenerated carriers.[53] After the combination of ZnO and $ZnIn_2S_4$, the emission peak intensities associated with their individual components in the ZZ8 heterojunction are significantly reduced. This is a clear indication that the heterojunction effectively inhibits the recombination of photogenerated carriers, which in turn boosts the efficiency of electron–hole separation. The improved photocatalytic performance of the ZZ8 composite is directly underpinned by its enhanced charge carrier separation efficiency, consistent with prior experimental data. To further elucidate the dynamics of photogenerated carrier transfer, we systematically analyzed the carrier lifetime (τ) using TRPL spectroscopy. As evidenced by the luminescence decay curves of the samples (Fig. S10) and corresponding carrier dynamics data (Table S4),[30,42,46] the average carrier lifetime of the ZZ8 heterojunction was prolonged to 5.11 ns, surpassing those of pure ZnO (4.39 ns) and $ZnIn_2S_4$ (3.68 ns). This indicates significantly improved separation and migration efficiency of photogenerated charges across the ZnO/$ZnIn_2S_4$ heterojunction interface. These experimental results clearly demonstrate that:(i) an efficient charge transfer pathway has been established between ZnO and $ZnIn_2S_4$;(ii) the interfacial electric field effect substantially suppresses the recombination loss of photogenerated carriers. These results offer compelling kinetic evidence for the pivotal role of heterojunction structures in enhancing photocatalytic performance. Subsequently, we employed the LSV test to evaluate the reduction capability of the samples.[49,54,55] As illustrated in Fig. 5(d), the ZZ8 composite requires a significantly lower overpotential than pure ZnO and

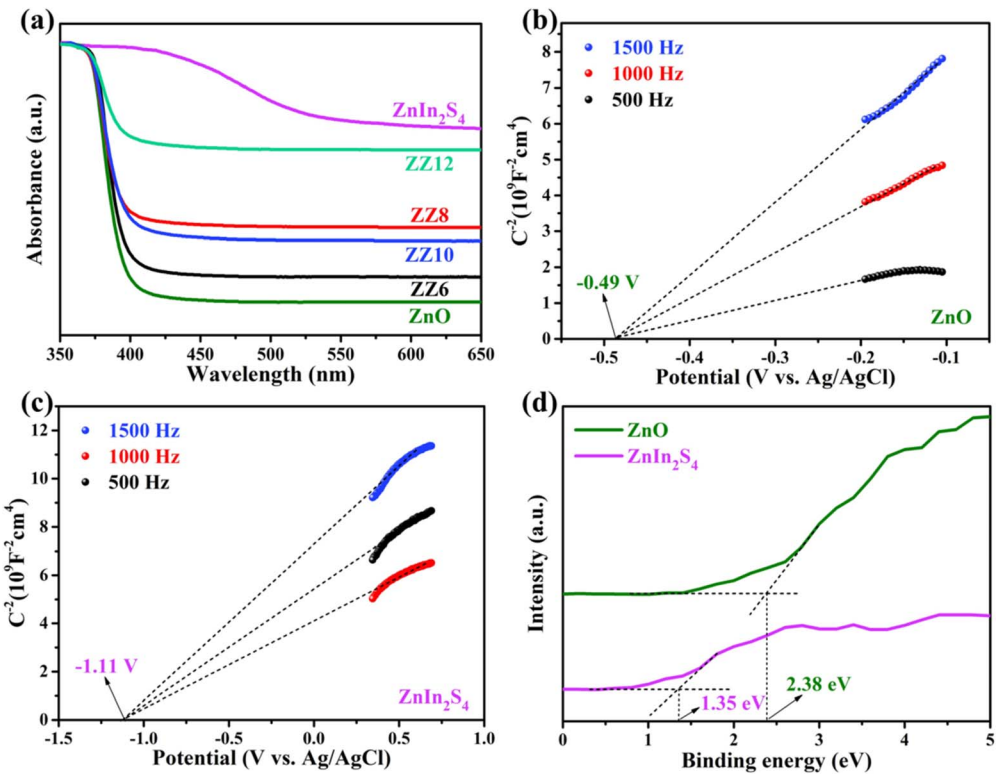

Fig. 6 (a) UV-vis DRS spectra, (b and c) Mott–Schottky plots, and (d) XPS valence band spectra of the samples.

$ZnIn_2S_4$ to achieve the same current density, demonstrating that reduction reactions occur more readily on the composite's surface compared to other samples. This characteristic is beneficial for the photoreduction of CO_2.

To investigate the light absorption properties of the samples, UV-vis DRS was performed. As shown in Fig. 6(a), pure ZnO exhibits strong light absorption in the ultraviolet region, with its absorption edge located around 400 nm. In contrast, pure $ZnIn_2S_4$ displays an absorption edge at approximately 540 nm, indicating its strong visible-light absorption capability. All ZnO/$ZnIn_2S_4$ composites exhibit a pronounced red-shift in their absorption edges relative to pure ZnO, which is attributed to the interfacial coupling effect between wide-bandgap ZnO and narrow-bandgap $ZnIn_2S_4$. Consequently, loading with $ZnIn_2S_4$ significantly broadens the composite's visible-light absorption range, thereby boosting their solar energy harvesting capability. The optical energy bandgaps (E_g) calculated through the Tauc plot analysis (Fig. S11(a)) are approximately 3.15 eV for ZnO and 2.23 eV for $ZnIn_2S_4$.[30,56,57]

Furthermore, the energy band structures were investigated by Mott–Schottky and XPS valence band tests. The Mott–Schottky plots (Fig. 6(b and c)) show positive slopes, confirming the characteristic of n-type semiconductors for ZnO and $ZnIn_2S_4$. The corresponding flat-band potentials (E_{FB}), derived from tangent fitting, are −0.49 V for ZnO and −1.11 V for $ZnIn_2S_4$ (*vs.* Ag/AgCl). Upon conversion to the standard hydrogen electrode scale, these E_{FB} values are −0.29 V and −0.91 V (*vs.* NHE), which are assigned as the E_f positions of pure ZnO and $ZnIn_2S_4$, respectively.[58,59] According to the XPS valence band spectra (Fig. 6(d)), the differences between the VB maxima and E_f are 2.38 eV for ZnO and 1.35 eV for $ZnIn_2S_4$, suggesting that their VB maxima are positioned at approximately +2.09 V and +0.44 V (*vs.* NHE), respectively. Combined with the E_g values (Fig. S11(a)), these VB values are used to calculate the CB minima of ZnO and $ZnIn_2S_4$ as −1.06 V and −1.79 V, respectively. Based on these derived energy levels, a schematic band structure diagram for both materials is proposed in Fig. S11(b).

3.4 CO_2 photoreduction mechanism analysis

To gain insights into the charge transfer pathway during photocatalysis, the ESR spectroscopy test was conducted. Using 5,5-dimethyl-1-pyrroline *N*-oxide (DMPO) as a radical trapping agent, we analyzed the radicals generated on the surfaces of pure ZnO, $ZnIn_2S_4$, and ZZ8 catalysts under light irradiation. As shown in Fig. 7, after 10 min of xenon lamp irradiation, all three samples exhibit six characteristic peaks for DMPO–$^{\bullet}O_2^-$ and four for DMPO–$^{\bullet}$OH. In composite systems, the efficiency of charge separation and the direction of transfer largely depend on the band positions of the constituent semiconductors. As shown in Fig. S11(b), pure ZnO and $ZnIn_2S_4$ exhibit staggered band structures. Their CB potentials (−1.06 V and −1.79 V) are sufficiently negative to reduce O_2 to $^{\bullet}O_2^-$ ($^{\bullet}O_2^-/O_2\cdot = -0.33$ V *vs.* NHE).[20] The enhanced DMPO–$^{\bullet}O_2^-$ signal of $ZnIn_2S_4$ confirms its superior reducing capability. The VB potential of $ZnIn_2S_4$ (+0.44 V) is insufficient to oxidize OH^- to $^{\bullet}$OH ($^{\bullet}OH/OH^- =$ +1.99 V *vs.* NHE). While only a weak DMPO–$^{\bullet}$OH signal is observed in pure $ZnIn_2S_4$ due to the partial conversion of $^{\bullet}O_2^-$,[60] ZnO exhibits a much stronger signal. This is because its VB potential (+2.09 V) is positive enough to thermodynamically favor the direct formation of $^{\bullet}$OH, demonstrating a superior oxidizing capability.

Among the three samples, the ZZ8 composite exhibits the most intense DMPO–$^{\bullet}O_2^-$ and DMPO–$^{\bullet}$OH ESR signals, indicating the highest yield of reactive radicals. This superior

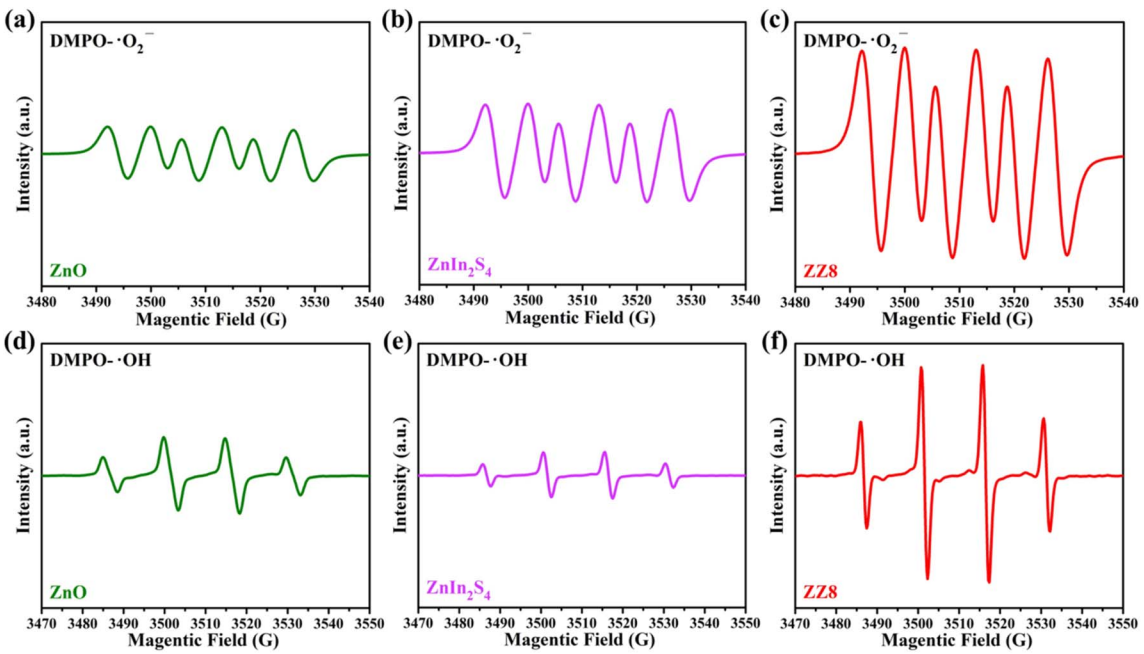

Fig. 7 ESR spectra for DMPO–$^{\bullet}O_2^-$ (a–c) and DMPO–$^{\bullet}$OH (d–f) of the samples.

activity stems from the effective coupling between ZnO and $ZnIn_2S_4$, which enables directional electron transfer from the CB of ZnO to the VB of $ZnIn_2S_4$ across the interface, thereby promoting the separation of photogenerated charges and subsequent radical generation. Such reverse electron transfer enables the effective recombination of useless charges, mainly retaining the photogenerated holes in the VB of ZnO with a higher oxidation potential, while the CB of $ZnIn_2S_4$ accumulates strongly reducing electrons. This effective spatial separation of photogenerated electron–hole pairs means that the charges in the ZZ8 composite follow an S-scheme heterojunction mechanism,[26] rather than a type-II pathway, thereby exhibiting the strongest photocatalytic CO_2 reduction activity.

It is widely recognized that the photocatalytic reduction of CO_2 proceeds *via* a two-stage process, beginning with continuous adsorption and followed by activation. To gain in-depth understanding of its reaction mechanism, we employed *in situ* FTIR to monitor the formation of intermediates in real time during the photoreduction CO_2 process on the ZZ8 catalyst. Dynamic monitoring was performed every 5 min in a pure water system under Xe-lamp irradiation. As shown in Fig. 8(a), the spectra display characteristic peaks at 2343 and 2356 cm^{-1}, consistent with the continuous adsorption of CO_2 on the photocatalyst surface. The peak observed at 3370 cm^{-1} (Fig. S12(a)) indicates the presence of surface OH^- species. Meanwhile, the four distinct peaks between 3550 and 3800 cm^{-1} are identified as adsorbed H_2O (Fig. S12(b)).[61] These observations indicate the generation of abundant highly active radicals and the presence of H_2O molecules during the reaction. As shown in Fig. 8(b and c), the vibrational peaks at 1073/1417/1472/1715/1790, 1396/1621, 1508, and 1731 cm^{-1} are attributed to HCO_3^-, b-CO_3^{2-}, m-CO_3^{2-}, and c-CO_3^{2-}, respectively, originating from the reaction of CO_2 and H_2O. The characteristic peak at 1240 cm^{-1} arises from the active *CO_2^- intermediate, while the appearance of the CO_2^* intermediate at 1339 cm^{-1} indicated the activation of CO_2 through reaction.[62,63]

Additionally, characteristic vibrational peaks of critical intermediates such as COOH* (1362/1518/1576/1632/1680 cm^{-1}), CHO* (1085/1386 cm^{-1}), CH_2O* (1095/1265 cm^{-1}), CH_3O* (1051/1174/1749 cm^{-1}), and CH_3^* (1374/1435/1455 cm^{-1}) are detected, confirming the efficient conversion of adsorbed CO_2 molecules. Among these, COOH* is a crucial intermediate for the formation of CO and CH_4 products from CO_2, while CH_3^* serves as a key intermediate specifically for the formation of CH_4.[64] The absorption band observed at 2077 cm^{-1} in Fig. 8(d) corresponds to the CO* intermediate on ZZ8.[65] Generally, CO*

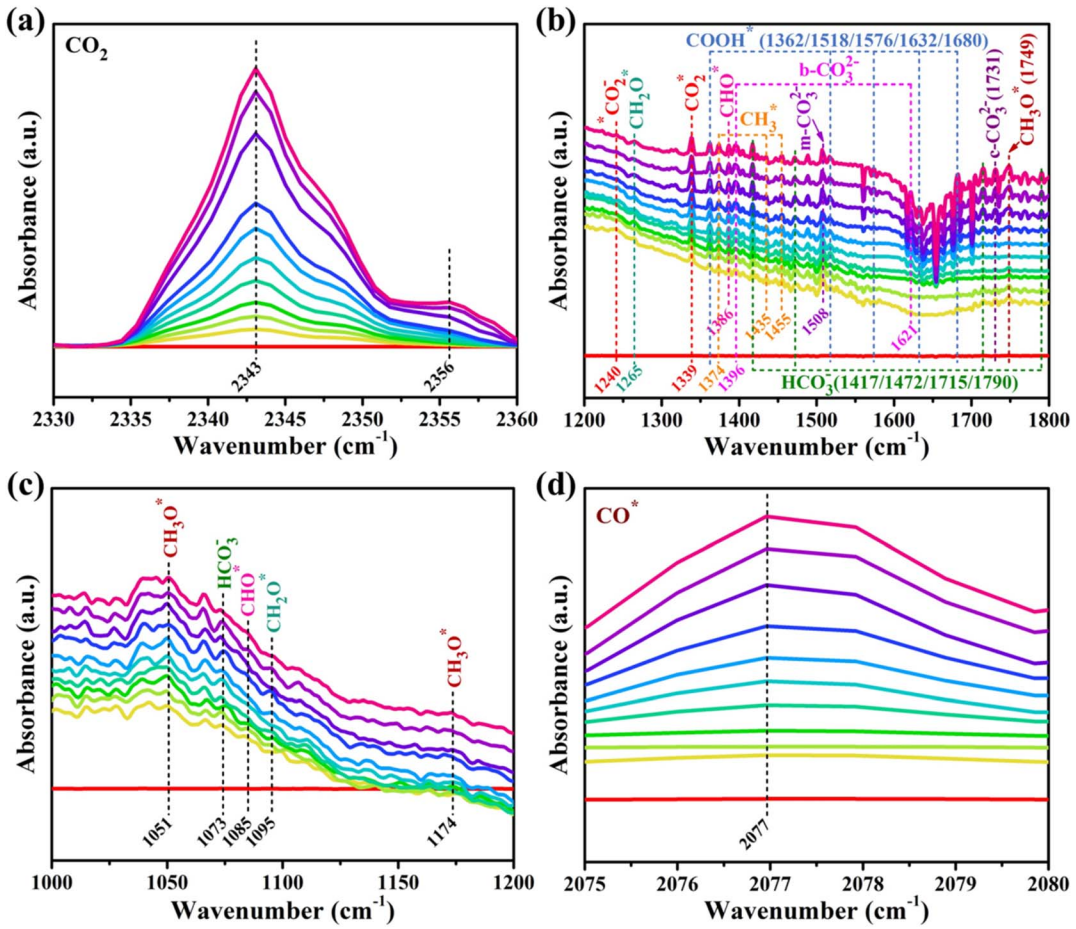

Fig. 8 *In situ* FTIR spectra of photocatalytic CO_2 reduction over ZZ8 in the regions of (a) 2330–2360 cm^{-1}, (b) 1200–1800 cm^{-1}, (c) 1000–1200 cm^{-1} and (d) 2075–2080 cm^{-1}.

tends to preferentially desorb and form free CO rather than undergo further protonation to produce CH_4, thus leading to higher CO yield than CH_4.[66] The conversion of CO_2 to CH_4 is an eight-electron reduction process. Under the influence of the S-scheme charge transfer pathway, a localized electron-rich microenvironment forms on the surface of the reduced semiconductor. This environment not only facilitates multi-electron reactions but also fine-tunes the adsorption strength of key intermediates (such as CO* and CHO*) on the catalyst surface, thereby significantly enhancing the efficiency of CO_2-to-CH_4 conversion.[42,67]

Guided by the experimental evidence above, we propose a charge transfer mechanism for the ZnO/$ZnIn_2S_4$ composite during CO_2 photoreduction in Fig. 9(a). When $ZnIn_2S_4$ is loaded onto the ZnO surface, the Fermi level difference thermodynamically drives electron migration from $ZnIn_2S_4$ to ZnO, until an equilibrium state is reached. The peak shifts in the XPS spectra (Fig. 1(c–f)) clearly validate this electron migration process. This spontaneous charge redistribution establishes electron accumulation and depletion layers at the ZnO/$ZnIn_2S_4$ interface, resulting in an electron-rich (negative) ZnO surface and an electron-deficient (positive) $ZnIn_2S_4$ surface. Thus, an intrinsic IEF and the bandgap bonding between the two components are formed.[5] Meanwhile, this electron migration causes an upward band bending in $ZnIn_2S_4$ and a downward bending in ZnO. Under light irradiation, electrons are photoexcited from the VB to CB in both components, generating holes in their respective VBs. Driven by the IEF and coulombic forces, the photogenerated electrons in ZnO's downward-bent CB migrate toward $ZnIn_2S_4$, recombining with the photogenerated holes in $ZnIn_2S_4$'s upward-bent VB at the interface.[28] This selective charge recombination ultimately preserves highly reductive electrons in the CB of $ZnIn_2S_4$ and strongly oxidative holes in the VB of ZnO, achieving effective spatial charge separation. Through this S-scheme charge transfer mechanism, the ZnO/$ZnIn_2S_4$ composite demonstrates significantly enhanced performance in the CO_2 photoreduction.

The possible conversion pathways for CO_2 photoreduction over the ZnO/$ZnIn_2S_4$ heterojunction are illustrated in Fig. 9(b).[5,26,68] The process begins with the adsorption of CO_2 and H_2O molecules onto the catalyst surface, leading to the formation of distinct adsorbed structural units. Here, $ZnIn_2S_4$ in the composite interacts strongly with the carbon atom of CO_2 through its exposed bimetallic sites, effectively weakening the

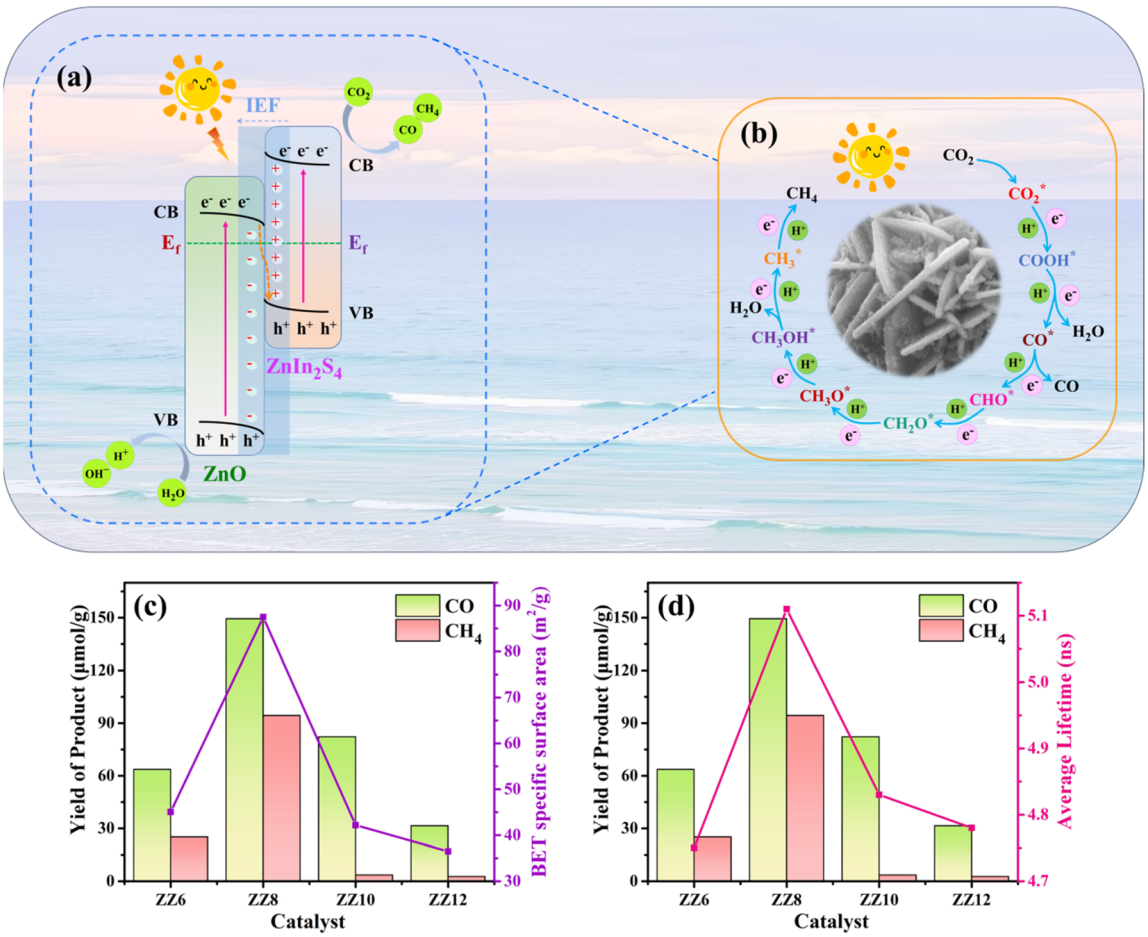

Fig. 9 Schematic diagram for (a) S-scheme charge transfer mechanism and (b) reaction pathway of CO_2 photoreduction over ZnO/$ZnIn_2S_4$; CO_2 photoreduction activity *versus* (c) the BET specific surface area and (d) the average lifetime of photogenerated carriers.

C=O double bond. Subsequently, under photoexcitation, the photogenerated electrons and holes cooperatively drive a multi-step proton-coupled electron transfer process. This process gradually reduces CO_2 molecules through intermediates such as COOH*, CO*, CHO*, CH_2O*, CH_3O*, CH_3OH*, and CH_3^*, ultimately yielding CO and CH_4.

The relationship between the photocatalytic CO_2 reduction performance and the BET specific surface area is shown in Fig. 9(c). The yields of CO and CH_4 exhibit a strong correlation with the BET specific surface area. As the loading amount of $ZnIn_2S_4$ increases, the BET specific surface area of the material gradually expands, thereby enhancing the CO_2 photoreduction performance of the ZnO/$ZnIn_2S_4$ composite. This can be mainly attributed to the larger specific surface area providing more adsorption sites and reaction sites for CO_2.[11,69] However, when an excessive amount of $ZnIn_2S_4$ is loaded, it blocks the material pores, leading to a reduction in the BET specific surface area and consequently a decrease in photocatalytic activity.

Fig. 9(d) illustrates the relationship between the photocatalytic CO_2 reduction performance and the average lifetime of photogenerated carriers. It can be observed that the ZZ8 sample exhibits the longest carrier lifetime and accordingly achieves the highest yields of CO and CH_4.[70] An appropriate loading of $ZnIn_2S_4$ effectively facilitates the separation of photogenerated electron–hole pairs in the ZnO/$ZnIn_2S_4$ composite, thereby prolonging the carrier lifetime and enhancing the photocatalytic CO_2 reduction activity.

4. Conclusion

In summary, an *in situ* growth strategy was employed to successfully construct a 3D/0D ZnO/$ZnIn_2S_4$ S-scheme heterojunction. SEM, TEM, and BET results demonstrated that the "nanoscale protrusions" formed by $ZnIn_2S_4$ NPs on the ZnO nanosheets, along with the Zn–In bimetallic active sites of $ZnIn_2S_4$, provided a multitude of active sites for promoting the adsorption and activation of CO_2 molecules. The spectroscopic (UV-vis DRS, PL) and electrochemical (EIS, TPR) analyses demonstrated that the effective loading of $ZnIn_2S_4$ NPs broadened the visible-light response, boosted CO_2 capture capacity, and facilitated the separation of photogenerated charge carriers in the ZZ8 composite. After 4 h of irradiation, the ZZ8 composite demonstrated dramatically higher product yields compared to its individual components. It produced 149.38 μmol g^{-1} of CO and 94.39 μmol g^{-1} of CH_4, which were 3.32 and 27.36 times greater than those of pure ZnO, and 3.44 and 5.51 times greater than those of pure $ZnIn_2S_4$, respectively. The ZZ8 composite maintained excellent performance, exceptional structural and chemical stability after ten reaction cycles. The establishment of an S-scheme heterojunction for charge transfer between ZnO and $ZnIn_2S_4$ was definitively established and confirmed through XPS and ESR. Concurrently, the reaction mechanism of the CO_2 reduction process was elucidated using *in situ* FTIR. Overall, this novel 3D/0D ZnO/$ZnIn_2S_4$ S-scheme heterojunction is a highly efficient and stable photocatalyst, indicating its promising potential for use in the field of photocatalysis.

Author contributions

Jiaze Wang: data curation, investigation, writing – original draft. Tongbin Zhang: data curation, investigation, writing – original draft. Xiaoyan Liu: conceptualization, formal analysis, project administration, resources, writing – review & editing. Lili Yang: supervision. Jian Cao: software, validation. Qiong Wu: software, visualization. Fengyou Wang: conceptualization, formal analysis. Yanli Chen: software, validation. Xin Li: investigation, methodology, writing – review & editing. Maobin Wei: conceptualization, supervision, visualization.

Conflicts of interest

There are no conflicts to declare.

Data availability

All relevant data are within the main article and supplementary information (SI). No additional data are available. All the data that support the findings of this study are available from the corresponding author upon reasonable request. Supplementary information: detailed testing procedures, instrument models and manufacturers, and supplementary data. See DOI: **https://doi.org/10.1039/d5ra06450c**.

Acknowledgements

This work is supported by the Program for the development of Science and Technology of Jilin province (Item No. YDZJ202501ZYTS348), the Program for the Science and Technology of Education Department of Jilin Province (Item No. JJKH20240568KJ), the National Youth Program Foundation of China (Grant No. 61705079).

References

1 Y. M. Cai, C. B. Lin, X. W. Cha, Y. L. Wu, X. P. Rao, K. B. Tan, D. R. Cai, G. L. Zhuang and G. W. Zhan, *ACS Catal.*, 2024, **14**, 8463–8479.
2 L. Y. Chen, B. H. Wu, X. R. Wu, D. H. Kuo, T. L. Wan, B. Q. Yang, P. K. Zhang, Z. J. Su, J. G. Lin, D. F. Lu and X. Y. Chen, *Int. J. Hydrogen Energy*, 2025, **98**, 944–956.
3 C. Du, X. Wang, W. Chen, S. Feng, J. Wen and Y. A. Wu, *Mater. Today Adv.*, 2020, **6**, 100071.
4 M. Akhlaq, C. Zhang, H. F. Yan, M. X. Ou, W. C. Zhang, S. W. Liang and R. M. A. Ikram, *Int. J. Agric. Biol. Eng.*, 2022, **15**, 51–59.
5 X. Liu, Y. C. Su, Y. D. Li, Q. H. Ma and J. H. Luo, *Small*, 2025, **21**, 2410721.
6 W. J. Li, Y. P. Zhang, Y. H. Wang, W. G. Ran, Q. H. Guan, W. C. Yi, L. L. Zhang, D. P. Zhang, N. Li and T. J. Yan, *Appl. Catal., B*, 2024, **340**, 123267.
7 T. A. Saleh, *RSC Adv.*, 2022, **12**, 23869–23888.
8 Y. J. Ren, J. J. Foo, D. Q. Zeng and W. J. Ong, *Small Struct.*, 2022, **3**, 2200017.

9 J. S. Chen, F. Xin, X. H. Yin, T. Y. Xiang and Y. W. Wang, *RSC Adv.*, 2015, **5**, 3833–3839.
10 L. Xu, J. J. Sun, Y. X. Zhang, W. Guo and B. J. Liu, *ACS Appl. Energy Mater.*, 2025, **8**, 12303–12315.
11 H. Q. Sun and S. B. Wang, *Energy Fuels*, 2014, **28**, 22–36.
12 J. G. He, G. G. Zhang, Y. C. Jiang, J. F. Jia and J. L. Cao, *Prog. Nat. Sci.:Mater. Int.*, 2023, **33**, 607–615.
13 W. Chen, T. Y. Liu, T. Huang, X. H. Liu and X. J. Yang, *Nanoscale*, 2016, **8**, 3711–3719.
14 J. Y. Liu, M. Liu, S. B. Zheng, X. Y. Liu, S. Y. Yao, F. Y. Jing and G. Chen, *J. Colloid Interface Sci.*, 2023, **635**, 284–294.
15 Y. Wu, Y. Yang, M. L. Gu, C. B. Bie, H. Y. Tan, B. Cheng and J. S. Xu, *Chin. J. Catal.*, 2023, **53**, 123–133.
16 A. Xu, Y. K. Zhang, H. G. Fan, X. Y. Liu, F. Y. Wang, X. Qu, L. L. Yang, X. Li, J. Cao and M. B. Wei, *ACS Appl. Nano Mater.*, 2024, **7**, 3488–3498.
17 W. A. Thompson, A. Olivo, D. Zanardo, G. Cruciani, F. Menegazzo, M. Signoretto and M. M. Maroto-Valer, *RSC Adv.*, 2019, **9**, 21660–21666.
18 P. K. Zhang, Q. H. Wu, H. Y. Wang, D. H. Kuo, Y. J. Lai, D. F. Lu, J. Q. Li, J. G. Lin, Z. H. Yuan and X. Y. Chen, *Chin. J. Catal.*, 2025, **74**, 279–293.
19 L. Zhang, Y. Hu, X. Wang, A. Zhang, X. L. Gao, A. E. A. Yagoub, H. L. Ma and C. S. Zhou, *Foods*, 2022, **11**, 1656.
20 Z. Y. Xie, L. J. Xie, F. F. Qi, H. Z. Liu, L. Y. Meng, J. L. Wang, Y. M. Xie, J. Chen and C. Z. Lu, *J. Colloid Interface Sci.*, 2023, **650**, 784–797.
21 K. S. Ranjith, A. Senthamizhan, B. Balusamy and T. Uyar, *Catal. Sci. Technol.*, 2017, **7**, 1167–1180.
22 X. R. Wu, T. L. Wan, B. Q. Yang, D. H. Kuo, P. K. Zhang, M. H. Liu, S. N. Adawara, D. F. Lu, J. G. Lin and X. Y. Chen, *J. Mater. Chem. A*, 2025, **13**, 17976–17991.
23 X. J. Luo, Z. Lou, L. L. Wang, X. J. Zheng and T. Zhang, *New J. Chem.*, 2014, **38**, 84–89.
24 A. F. Zhu, T. H. Jiao, S. Ali, Y. Xu, Q. Ouyang and Q. S. Chen, *Food Chem.*, 2022, **391**, 133277.
25 Y. J. Wang, H. G. Fan, X. Y. Liu, J. Cao, H. L. Liu, X. Li, L. L. Yang and M. B. Wei, *J. Alloys Compd.*, 2023, **945**, 169197.
26 Y. N. Zhang, M. Y. Xu, W. Q. Zhou, X. H. Song, X. Liu, J. S. Zhang, S. T. Chen and P. W. Huo, *J. Colloid Interface Sci.*, 2023, **650**, 1762–1772.
27 J. M. Li, C. C. Wu, J. Li, B. H. Dong, L. Zhao and S. M. Wang, *Chin. J. Catal.*, 2022, **43**, 339–349.
28 R. Z. Xiong, X. X. Ke, W. F. Jia, Y. H. Xiao, B. C. Cheng and S. J. Lei, *J. Mater. Chem. A*, 2023, **11**, 2178–2190.
29 W. Liu, E. N. Ha, L. Y. Wang, L. S. Hu, L. Y. S. Lee and K. Y. Wong, *Adv. Mater. Interfaces*, 2018, **5**, 1800611.
30 R. Wang, X. Y. Xie, C. X. Xu, R. D. Ji, Z. L. Shi, Q. N. Cuia and M. L. Wang, *Catal. Sci. Technol.*, 2023, **13**, 426–436.
31 L. B. Wang, B. Cheng, L. Y. Zhang and J. G. Yu, *Small*, 2021, **17**, 2103447.
32 H. M. Yu, S. H. Guo, M. L. Jia, J. C. Jia, Y. Chang and J. Wang, *Arabian J. Chem.*, 2024, **17**, 105975.
33 J. J. Wang, L. Huang, B. J. Sun, H. F. Zhang, D. F. Hou, X. Q. Qiao, H. J. Ma and D. S. Li, *Chem. Eng. J.*, 2024, **479**, 147719.
34 H. Liu, Z. T. Jin, Z. Z. Xu, Z. Zhang and D. Ao, *RSC Adv.*, 2015, **5**, 97951–97961.
35 S. P. Wan, M. Ou, Q. Zhong, S. L. Zhang and F. J. Song, *Chem. Eng. J.*, 2017, **325**, 690–699.
36 G. R. S. Andrade, C. C. Nascimento, Z. M. Lima, E. T. Neto, L. P. Costa and I. F. Gimenez, *Appl. Surf. Sci.*, 2017, **399**, 573–582.
37 S. H. Chen, X. L. Zhao, F. Z. Xie, Z. Tang and X. F. Wang, *New J. Chem.*, 2020, **44**, 7350–7356.
38 R. Wang, L. J. Zhao, L. Li, Q. Song and J. W. Huang, *J. Phys. Chem. Solids*, 2020, **136**, 109148.
39 H. B. Yu, J. N. Liu, X. Y. Li, Y. T. Li, J. Wang, D. D. Wang, J. H. Lang, J. H. Yang and H. X. Lan, *J. Mater. Sci.: Mater. Electron.*, 2021, **32**, 20082–20092.
40 Z. X. Bi, R. T. Guo, X. Hu, J. Wang, X. Chen and W. G. Pan, *Energy & Fuels*, 2023, **37**, 6036–6048.
41 X. Li, A. Xu, H. G. Fan, X. Y. Liu, J. Wang, J. Cao, L. L. Yang and M. B. Wei, *J. Power Sources*, 2022, **545**, 231923.
42 Y. X. Sun, K. Z. Lai, X. Q. Shi, N. Li, Y. Q. Gao and L. Ge, *Appl. Catal., B*, 2025, **365**, 124907.
43 Z. J. Su, B. H. Wu, C. Z. Li, D. H. Kuo, P. K. Zhang, L. Y. Chen, D. F. Lu, J. G. Lin, X. Y. Chen and Z. H. Yuan, *Chem. Eng. J.*, 2025, **510**, 161621.
44 Z. J. Su, X. R. Wu, D. H. Kuo, B. Q. Yang, B. H. Wu, L. Y. Chen, P. K. Zhang, J. G. Lin, D. F. Lu and X. Y. Chen, *J. Mater. Chem. A*, 2024, **12**, 10494–10506.
45 X. Y. Chen, P. K. Zhang, D. H. Kuo, Q. H. Wu, A. B. Abdeta, B. H. Wu, Z. J. Su, L. Y. Chen, O. A. Zelekew and J. G. Lin, *J. Mater. Chem. A*, 2023, **11**, 19091–19106.
46 F. Z. Zeng, Y. J. Chen, L. Kan, L. Liu, J. J. Zhang and G. H. Tian, *Sep. Purif. Technol.*, 2025, **356**, 129870.
47 Y. Dai, W. G. Peng, Y. Ji, J. Wei, J. H. Che, Y. Q. Huang, W. H. Huang, W. M. Yang and W. Z. Xu, *J. Food Sci.*, 2024, **89**, 8022–8035.
48 Z. Zhang, F. H. Kong, B. Z. Yuan, Y. N. Liao, X. Ren and Y. Hou, *RSC Adv.*, 2023, **13**, 17362–17369.
49 H. Z. Deng, X. G. Fei, Y. Yang, J. J. Fan, J. G. Yu, B. Cheng and L. Y. Zhang, *Chem. Eng. J.*, 2021, **409**, 127377.
50 S. Yang, Y. S. Qi, C. F. Wang, Y. Y. Liu, X. P. Zhang, D. L. Han and H. G. Wang, *J. Colloid Interface Sci.*, 2025, **699**, 138147.
51 Q. Y. Zhang, L. H. Huang, S. F. Kang, C. C. Yin, Z. Ma, L. F. Cui and Y. G. Wang, *RSC Adv.*, 2017, **7**, 43642–43647.
52 A. Sabbah, I. Shown, M. Qorbani, F. Y. Fu, T. Y. Lin, H. L. Wu, P. W. Chun, C. I. Wu, S. R. M. Santiago, J. L. Shen, K. H. Chen and L. C. Chen, *Nano Energy*, 2022, **93**, 106809.
53 S. J. Wang, F. T. He, X. L. Zhao, J. Q. Zhang, Z. M. Ao, H. Wu, Y. Yin, L. Shi, X. Y. Xu, C. C. Zhao, S. B. Wang and H. Q. Sun, *Appl. Catal., B*, 2019, **257**, 117931.
54 P. Tian, H. G. Fan, X. Y. Liu, Q. Wu, J. Cao, L. L. Yang, X. Li, M. B. Wei and B. R. Li, *Sep. Purif. Technol.*, 2025, **356**, 129967.
55 P. Zhang, J. Cao, Q. Wu, X. F. Li, L. Fan, L. L. Yang, M. B. Wei, J. H. Yang, X. Li and B. R. Li, *Colloids Surf., A*, 2025, **705**, 135573.
56 D. D. Liu, L. P. Jiang, D. Q. Chen, Z. K. Hao, B. W. Deng, Y. Y. Sun, X. Liu, B. Y. Jia, L. M. Chen and H. T. Liu, *ACS Catal.*, 2024, **14**, 5326–5343.

57 X. Y. Bi, L. B. Li, L. J. Luo, X. H. Liu, J. M. Li and T. Y. You, *Food Chem.*, 2022, **385**, 132657.
58 J. Y. Tang, R. T. Guo, W. G. Zhou, C. Y. Huang and W. G. Pan, *Appl. Catal., B*, 2018, **237**, 802–810.
59 Y. Bai, L. Q. Ye, T. Chen, L. Wang, X. Shi, X. Zhang and D. Chen, *ACS Appl. Mater. Interfaces*, 2016, **8**, 27661–27668.
60 F. He, B. C. Zhu, B. Cheng, J. G. Yu, W. K. Ho and W. Macyk, *Appl. Catal., B*, 2020, **272**, 119006.
61 J. Li, W. F. Pan, Q. Y. Liu, Z. Q. Chen, Z. J. Chen, X. Z. Feng and H. Chen, *J. Am. Chem. Soc.*, 2021, **143**, 6551–6559.
62 X. Y. Wan, Y. F. Li, Y. H. Chen, J. Ma, Y. A. Liu, E. D. Zhao, Y. D. Gu, Y. L. Zhao, Y. Cui, R. T. Li, D. Liu, R. Long, K. M. Liew and Y. J. Xiong, *Nat. Commun.*, 2024, **15**, 1273.
63 Y. Y. Qin, Y. Wang, J. Lu, L. L. Xu and W. Y. Wong, *Angew. Chem., Int. Ed.*, 2025, **64**, e202418269.
64 H. N. Shi, Y. Liang, J. G. Hou, H. Z. Wang, Z. H. Jia, J. M. Wu, F. Song, H. Yang and X. W. Guo, *Angew. Chem., Int. Ed.*, 2024, **63**, e202404884.
65 W. Geng, Y. Y. Xiong, C. X. Chen, S. L. Ning, Z. Xiong, S. L. Deng, Y. X. Tan, X. M. Song, M. Pan, M. Mayor and C. Y. Su, *Angew. Chem., Int. Ed.*, 2025, **64**, e202505546.
66 X. Li, W. M. He, C. H. Li, B. Song and S. W. Liu, *Appl. Catal., B*, 2021, **287**, 119934.
67 Z. Tang, F. F. Zhu, J. C. Zhou, W. S. Chen, K. Wang, M. C. Liu, N. Wang and N. X. Li, *Appl. Catal., B*, 2022, **309**, 121267.
68 K. Z. Lai, Y. X. Sun, N. Li, Y. Q. Gao, H. Li, L. Ge and T. Y. Ma, *Adv. Funct. Mater.*, 2024, **34**, 2409031.
69 L. Y. Chen, P. K. Zhang, D. H. Kuo, J. M. Jiang, B. H. Wu, Z. J. Su, O. A. Zelekew, J. G. Lin, D. F. Lu and X. Y. Chen, *J. Mater. Chem. A*, 2024, **12**, 9871–9885.
70 B. Q. Yang, X. Wu, B. K. Inusa, D. H. Kuo, P. K. Zhang, C. Z. Li, T. Liu, D. F. Lu, Z. H. Yuan, J. G. Lin and X. Y. Chen, *Chem. Eng. J.*, 2025, **514**, 163151.